



HAL
open science

Dynamic Characterization of Inter- and Intralamellar Domains of Cobalt-Based Layered Double Hydroxides upon Electrochemical Oxidation

Christine Taviot-Guého, Pierre Vialat, Fabrice Leroux, Fatemeh Razzaghi, Hubert Perrot, Ozlem Sel, Nicholai Daugaard Jensen, Ulla Gro Nielsen, Sophie Peulon, Erik Elkaim, et al.

► **To cite this version:**

Christine Taviot-Guého, Pierre Vialat, Fabrice Leroux, Fatemeh Razzaghi, Hubert Perrot, et al.. Dynamic Characterization of Inter- and Intralamellar Domains of Cobalt-Based Layered Double Hydroxides upon Electrochemical Oxidation. *Chemistry of Materials*, 2016, 28 (21), pp.7793-7806. 10.1021/acs.chemmater.6b03061 . hal-01416181

HAL Id: hal-01416181

<https://hal.sorbonne-universite.fr/hal-01416181>

Submitted on 1 Sep 2022

HAL is a multi-disciplinary open access archive for the deposit and dissemination of scientific research documents, whether they are published or not. The documents may come from teaching and research institutions in France or abroad, or from public or private research centers.

L'archive ouverte pluridisciplinaire **HAL**, est destinée au dépôt et à la diffusion de documents scientifiques de niveau recherche, publiés ou non, émanant des établissements d'enseignement et de recherche français ou étrangers, des laboratoires publics ou privés.



Distributed under a Creative Commons Attribution - NonCommercial 4.0 International License

Dynamic Characterization of Inter- and Intralamellar Domains of Cobalt-Based Layered Double Hydroxides upon Electrochemical Oxidation

Christine Taviot-Guého,^{*,†} Pierre Vialat,[†] Fabrice Leroux,[†] Fatemeh Razzaghi,[‡] Hubert Perrot,^{*,‡} Ozlem Sel,[‡] Nicolai Daugaard Jensen,[⊥] Ulla Gro Nielsen,[⊥] Sophie Peulon,[§] Erik Elkaim,^{||} and Christine Mousty^{*,†}

[†]Université Blaise Pascal, Institut de Chimie de Clermont-Ferrand, ICCF UMR CNRS 6296, BP 10448, Université Clermont Auvergne, F-63000 Clermont-Ferrand, France

[‡]CNRS, Laboratoire Interfaces et Systèmes Electrochimiques, UPMC Université Paris 06, Sorbonne Universités, 4 place Jussieu, F-75005, Paris, France

[§]CNRS UMR 8587, Laboratoire Analyse et Modélisation pour la Biologie et l'Environnement, Université Evry, Boulevard François Mitterrand, F-91025 Cedex Evry, France

^{||}Synchrotron SOLEIL, F-91190 Cedex Gif-sur-Yvette, France

[⊥]Department of Physics, Chemistry and Pharmacy, University of Southern Denmark, Campusvej 55, 5230 Odense Municipality, Denmark

ABSTRACT: This work investigated in situ changes in the structure of the layered double hydroxides (LDH) during electrochemical processes as well as followed the ion motion related to the charge balancing process. Electrogravimetric measurements, using an electro-chemical quartz crystal microbalance (EQCM), allowed one to monitor simultaneously changes in current and in microbalance frequency when electroactive films of Co₂Al-NO₃ LDH were subjected to voltammetry potential cycling in alkaline solutions (0.1 M COH, C = Li⁺, Na⁺, and K⁺). EQCM results showed a strong dependence of the electrochemical process on the nature of electrolyte cations. Operando X-ray diffraction measurements, carried out during potential cycling of Co₂Al-NO₃ films in KOH electrolyte, showed the diffusion of OH⁻ species gradually replacing NO₃⁻. Total X-ray scattering experiments recorded ex situ on Co₂Al-NO₃ after successive oxidation and reduction revealed the presence of a high level of structural disorders even in the pristine material. A quantitative analysis of the local distribution of the cations by the analysis of the pair distribution functions highlighted the presence of different Co sites with distinct modification of Co-OH distances in the first coordination shells after oxidation/reduction.

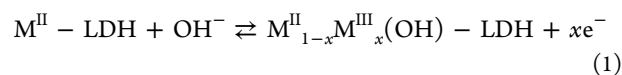
1. INTRODUCTION

With the increasing demand of ecofriendly energy resources, supercapacitors are advantageously positioned between capacitors and batteries as fast power delivering systems. Indeed, high energy density, high power density, and excellent cycling lifespan are required for new applications such as electrical vehicles and other devices requiring transportable energy.^{1,2} According to the mechanisms involved in energy storage, supercapacitors can be divided into two categories, either (i) superficial, so-called electrochemical double layer capacitors, or (ii) multielectron-transfer faradic reaction with fast charge discharge properties, so-called pseudocapacitors or redox capacitors. Recently, two-dimensional materials, such as layered double hydroxides (LDH), have attracted increasing interest for their pseudocapacitive properties.³⁻⁵

Layered double hydroxides, also referred to as anionic clays or hydroxalite-like compounds, consist of M^{II}(OH)₆ and M^{III}(OH)₆ edge-sharing octahedra that form sheets similar to those of brucite. The general formula [M²⁺_{1-a}M³⁺_a(OH)₂]^{a+}[(Aⁿ⁻)_{a/n}·yH₂O] is usually abbreviated as M²⁺_RM³⁺_{1-R}A, where R corresponds to the molar ratio of the divalent M²⁺ to trivalent M³⁺ metal cations with a substitution rate of M²⁺ by M³⁺ cations, and Aⁿ⁻ is the interlayer anion. The LDH structure consists of positively charged brucite-like layers, whose net charge is compensated for by anions located in the interlayers, which can easily exchange. LDH have thus been widely

investigated because of the broad versatility of their metal layer composition, their anionic exchange properties, and their varied morphologies, making them interesting materials for various applications.⁶ For instance, the relevance of LDH as electrode modifiers for electrochemical detection, biosensing, and energy storage (supercapacitors and batteries) has been recently reviewed.^{3–5,7} Interestingly, 3d-metal M cations can endow redox properties to the LDH layer structure that may open new possibilities with regard to energy storage. For instance, cobalt-containing LDH materials are generally reported to have better pseudocapacitive performances in comparison to the nickel-based LDH.^{3–5}

Classically, the redox process in 3d M-LDH may be depicted by the following reaction:



However, while the charge-transfer mechanism within LDH looks simple, the understanding of the role of metallic active sites as well as the ion motion in the electron transportation mechanism and surface reactions is very challenging to optimize their electrochemical properties.⁸ Indeed, the propagation of a redox reaction through microcrystals immobilized at the electrode proceeds *via* a mixed electron and ionic transport.⁹ An electroactive component in the inorganic LDH layer can be oxidized or reduced if the transfer of electrons is simultaneously followed by the insertion or expulsion of ions. In particular for NiAl-LDH, a dependence of the electrochemical signal on the electrolyte cations (K^{+} , Na^{+} , or Li^{+}) suggests that they are involved in the charge neutralization process.^{10,11} However, conventional electrochemical methods, *i.e.*, cyclic voltammetry (CV) or electrochemical impedance spectroscopy (EIS) alone, do not provide information on the exact identification of the ionic species involved in the insertion/deinsertion phenomena accompanying the electron transfer. It is therefore challenging to find eligible techniques for the study of *in situ* modifications of a Co-based LDH layer structure upon oxidation process as well as to monitor ion motion. These two aspects will be investigated in the present work, first on one hand by quartz crystal microbalance (QCM) measurements for ion motion and second through high resolution synchrotron X-ray measurements for structural modifications.

Interestingly, few examples have recently initiated the use of QCM as an *in situ* gravimetric probe to study LDH-based electrodes.^{10,12–14} This methodology involves the use of electrodes coated on the QCM resonators as working electrodes in an electrochemical cell. Consequently, the coupling of CV with QCM measurements provides the information on the mass variations (calculated from the Sauerbrey equation,¹⁵ eq 2) occurring at the electrode surface during electrochemical processes.^{16,17} In the present work, the coupled CV/QCM methodology, also called cyclic electrogravimetry, was exploited to study the electrochemical behavior of Co_2Al-NO_3 LDH films. Special attention was paid to the poorly understood aspects, such as the nature of the ions involved in the charge compensation process by varying the sizes of electrolyte cations, namely, K^{+} , Na^{+} , Li^{+} , and their possible solvated forms.

In order to probe the structural effects on LDH framework that may occur during the electrochemical treatment, high resolution synchrotron X-ray measurements were carried out. *Operando* X-ray diffraction measurements using an electro-

chemical cell placed on the synchrotron beam show few changes over a long distance during the electrochemical treatment except for a modification of the interlayer content. On the other hand, the pair distribution functions (PDFs), obtained from total X-ray scattering experiments and performed on *ex situ* samples, which have been oxidized or reduced at fixed potential, reveal important modifications of the LDH hydroxide layer structure both in the short and medium ranges. A quantitative analysis of the local distribution of the cations and the modification of M–OH distances for the first coordination shells after oxidation and reduction are offering both new insights and approaches for understanding the electrochemical properties of these LDH materials.

2. EXPERIMENTAL SECTION

2.1. Chemicals. The following chemicals were used to prepare and characterize LDH thin films: $Al(NO_3)_3 \cdot 9H_2O$ (Acros, 99%), $Co(NO_3)_2 \cdot 6H_2O$ (Acros, 99%), NaOH (VWR, 99%, CE), $LiOH \cdot H_2O$ (Sigma-Aldrich, 98%, St. Louis, MO, USA), and KOH (Sigma-Aldrich, 98%) which were used as received without further purification. Deionized water was employed for all of the experiments.

2.2. Synthesis. Co_2Al-NO_3 LDH were prepared under similar experimental conditions, by the coprecipitation route in fast mode, previously described in detail by Vialat et al.¹¹ A 25 mL aliquot of the nitrate salts ($Co(NO_3)_2$ and $Al(NO_3)_3$) solution was prepared with a total cationic concentration of 0.1 M and respecting the molar ratio $M^{II}/Al = 2$. The nitrate salt solution was then added dropwise into a reactor with a constant flow of 0.275 mL/min. The pH was maintained at a constant value of 9.5 by the simultaneous addition of a 0.2 M NaOH solution. The reaction was carried out under N_2 atmosphere to avoid carbonate anion contamination. The addition of the nitrate salt solution was complete within 3 h, and the suspensions were immediately centrifuged at 4500 rpm without any aging in order to quench the crystal growth and therefore obtain small platelets. The solids recovered by centrifugation were washed three times with deionized water and dried in air at 30 °C overnight. ICP-AES analysis confirms the LDH formation with a Co^{II}/Al molar ratio of 1.99.

Two additional samples were prepared for *ex-situ* XRD and FTIR characterizations through the electrolysis of the above Co_2Al-NO_3 sample at constant potential to oxidize or reduce Co species. To do so, 2 × 100 mg of LDH powder were separately suspended in a 0.1 M KOH solution and oxidized for 1 h at a potential of 0.8 V/SCE under stirring for the first one ($Co_2Al-NO_3(ox)$) and then reduced for 1 h at 0.0 V/SCE for the second sample ($Co_2Al-NO_3(ox/red)$). The solids were finally recovered by centrifugation and washed with water, and once dried they were placed in a capillary for XRD analysis. Infrared spectra were recorded in transmission mode using the KBr pellet technique with a Nicolet 5700 spectrometer from Thermo Scientific.

2.3. Preparation of Thin LDH Films. LDH thin films were deposited on the gold electrode of quartz resonators ($A = 0.2 \text{ cm}^2$, 9 MHz, AWS, Spain). Before deposition, the gold electrode was properly rinsed with water and ethanol. A mother solution of 2.5 mg mL^{-1} LDH suspension was prepared in 2 mL of deionized water degassed by N_2 . This suspension was sonicated during 15 min and then diluted 10 times for reaching the mass concentration of 0.25 mg mL^{-1} . Subsequently, the as-prepared suspension was agitated overnight and then sonicated for 15 min before deposition of a volume equal to 50 $\mu\text{g cm}^{-2}$ on the gold electrode of quartz resonators to be finally dried in air. The morphology and the film thickness ($\approx 350 \text{ nm}$) were investigated by field emission gun scanning electron microscopy (FEG-SEM; Zeiss, Supra 55) (Figure.S1). Thin films, *i.e.*, sub-micrometer thickness values, were prepared; this consideration is used to maintain the gravimetric regime of the electrochemical quartz crystal microbalance (EQCM) and to avoid any mechanical contribution which can affect the EQCM response.¹⁸

2.4. Electrogravimetric Characterization. EQCM measurements were made using a BioLogic Science Instrument, SP-200, coupled with a laboratory-made QCM device. The electrochemical

experiments were performed in aqueous 0.1 M solutions of KOH, NaOH, and LiOH using a three-electrode cell, including gold-patterned quartz substrates of 9 MHz coated with LDH thin films as working electrodes. A platinum grid and a saturated calomel electrode (SCE) served respectively as the counter electrode and the reference electrode. During the electrochemical tests, a salt-bridge junction equipped with a porous glass frit on the end was used to prevent the reference electrode from being contaminated by the media and vice versa. Cyclic electrogravimetric measurements at different sweep rates (v) between 5 and 50 $\text{mV}\cdot\text{s}^{-1}$ were recorded over a potential window from 0.65 to 0.2 V/SCE. EQCM responses were recorded after the signal stabilization following an activation of the modified electrodes by potential cycling (5 cycles). Frequency changes, Δf_m , of the quartz crystal resonator were monitored during cyclic voltammetry measurements by a laboratory-made QCM device. The Δf_m can be converted into the mass change (Δm) of the quartz crystal by applying the Sauerbrey equation:⁸

$$\Delta m = -\frac{S\sqrt{\rho_q\mu_q}}{2f_0^2}\Delta f_m = -k_s\Delta f_m \quad (2)$$

where S is the active surface of the gravimetric sensor, ρ_q is the density of quartz ($2.648 \text{ g}\cdot\text{cm}^{-3}$), μ_q is the shear modulus of quartz ($2.947 \times 10^{11} \text{ g}\cdot\text{cm}^{-1}\cdot\text{s}^{-2}$), f_0 is the fundamental resonance frequency of the quartz, and k_s is the sensitivity factor. In this work, an experimental value of $1.09 \text{ ng}\cdot\text{Hz}^{-1}$, for an active surface of 0.2 cm^2 , was used as already justified in ref 19.

2.5. Structural Characterization. **2.5.1. Operando XRD Measurements.** Operando structural characterizations were carried out using a laboratory-made electrochemical flow cell especially developed for synchrotron measurements.²⁰ The reference electrode is an Ag/AgCl laboratory-made microelectrode (diameter = 3 mm; 0.1 $\text{mol}\cdot\text{L}^{-1}$ NaCl; $E_{\text{ref}} = 0.29 \text{ V/ESH}$). The counter electrode is a film of carbon-doped kapton (Goodfellow, $370 \Omega\cdot\text{cm}^{-2}$) which is transparent to X-rays. The working electrode is a glass plate covered with indium tin oxide (ITO SOLEMS, $30 \Omega\cdot\text{cm}^{-2}$) coated with a thin film of $\text{Co}_2\text{Al-NO}_3$ ($\approx 100 \mu\text{g}\cdot\text{cm}^{-2}$). The surface in contact with the electrolyte solution was equal to 3 cm^2 , and the cell volume was evaluated to $\sim 2 \text{ mL}$. The 0.1 M KOH electrolyte solution was introduced by a piloted piezoelectric micropump (flow rate $\sim 1.25 \text{ mL/min}$). Electrochemical measurements were performed at room temperature using a MicroAutolab potentiostat/galvanostat system (Eco Chemie). X-ray diffraction data were recorded operando, i.e., during the potential cycling between 0 and 0.7 V and reverse ($v = 1 \text{ mV}\cdot\text{s}^{-1}$ in 12 min) by placing the electrochemical cell on the synchrotron beam of wavelength 0.4388 Å (CRISTAL at Synchrotron Soleil, France) using an MAR345 imaging plate detector (2D) which allowed us to collect data in a few minutes but on a shorter $Q/2\theta$ range.

2.5.2. Total X-ray Scattering Experiments. Measurements were performed *ex situ* on the pristine $\text{Co}_2\text{Al-NO}_3$ sample, and the solids obtained after electrochemical treatments, i.e., $\text{Co}_2\text{Al-NO}_3(\text{ox})$ and $\text{Co}_2\text{Al-NO}_3(\text{ox/red})$, loaded in a rotating 0.7 mm diameter glass capillary, which was mounted on a two-circle diffractometer equipped with a 21 crystals multianalyzer crystal detector (CRISTAL at Synchrotron Soleil).

DIFFaX software²¹ was used to analyze the position and the profile of certain X-ray diffraction peaks (synchrotron data) for the $\text{Co}_2\text{Al-NO}_3$ *ex situ* sample. Radha and Kamath²² have provided the detailed steps for use of DIFFaX for the simulation of the powder X-ray diffraction patterns of LDHs. DIFFaX simulations were done at $\lambda = 0.4388 \text{ Å}$. The stacking unit comprising a metal hydroxide slab and an interlayer, and it was built by considering the atomic coordinates reported for $\text{Ni}_2\text{Al-CO}_3$ ²³ and $\text{Zn}_2\text{Al-NO}_3$.²⁴ The stacking vector ($2/3, 1/3, 1/3$) generates the $3R_1$ polytype. The $2H_1$ polytype is generated by defining two different layers AC and CA and then stacking them one atop another using the stacking vector $(0, 0, 1/2)$. For a comparison with experimental patterns, the calculated peaks were broadened using a Lorentzian profile function (full width at half-maximum) = $0.4^\circ (2\theta)$.

2.5.3. Analysis of Pair Distribution Functions. The PDF method is based on the total scattering pattern, in which both the Bragg peaks and the diffuse component are considered to reflect the average longer range atomic structure and the local structural imperfections.²⁵ The patterns were collected at the Synchrotron Soleil on CRISTAL beamline, using an incident wavelength of 0.4388 Å, covering a Q (scattering vector) range up to 25 Å^{-1} ($2\theta = 125^\circ$). Data were then computed using PDFgetX2²⁶ and PDFgetX3²⁷ software. First, data were corrected from sample holder contribution (which was determined using a separate diffraction measurement of an empty glass capillary), sample self-absorption, multiple scattering, and Laue diffuse; using 21 Si(111) crystal analyzers as a detector, Compton scattering correction is not necessary. Then, the corrected X-ray diffraction data $I(Q)$ was scaled into electron units, and the structure function $S(Q)$ was calculated. The PDF, which gives the probability of finding an atom at a distance r away from another atom, was obtained via the sine Fourier transform of the total scattering function $S(Q)$ according to the following equation:

$$G(r) = \frac{2}{\pi} \int_0^\infty Q[S(Q) - 1] \sin Qr \text{ d}Q \quad (3)$$

$S(Q)$ was truncated at $Q_{\text{max}} = 23 \text{ Å}^{-1}$, the signal-to-noise ratio being unfavorable beyond that value of Q .

In order to study the local structural modifications induced by the electrochemical treatment (*ex situ* experiments on $\text{Co}_2\text{Al-NO}_3$ samples), the PDF data were refined in real space in the space group $C2/m$ starting from the structure recently published by Marappa and Kamath²⁸ using the PDFGui software.²⁹ Refinements were done in the r range of 1.5–4.5/(6.0 Å), yielding information about the very local structure on the first M–OH and second M–M coordination shells around M cations. In the $C2/m$ asymmetric unit cell, the metal hydroxide layer is described by two cations M in the 2a and 4g special positions and two oxygen atoms (assimilated to OH group) at the 8j and 4i positions. The layers are stacked by a vector which is inclined to the plane of the metal hydroxide layer at $\beta \sim 103^\circ$. Co^{2+} was first placed in the 4g site and Al^{3+} in the 2a site leading to a Co/Al molar ratio of 2 consistently with the chemical analysis. Interlayer species, i.e., nitrate (two NO_3^- per formula unit $\text{Co}_4\text{Al}_2(\text{OH})_6$) or carbonate anions (1 CO_3^{2-}) and water molecules (two H_2O) were included in the refinement in order to accurately represent the average number density, but neither their positions nor the atomic displacement parameters ADP were refined. Only the lattice parameters a and b were refined; the value of β was set to 103° , and the value of c parameter was determined from the position of the 00l Bragg peaks. First, the coordinates of M cation and oxygen atoms within the hydroxide layer were refined separately taking into account the symmetry constraints. Then, the diagonal isotropic parameters (U_{11} , U_{22} , and U_{33}) of both the oxygen atoms and the cations were allowed to vary. The r dependence of the PDF peak widths (correlated atomic displacements) was accounted for by defining a low- r to high- r PDF peak ratio with a cutoff value of 3.3 Å for $\text{Co}_2\text{Al-NO}_3(\text{ox})$ and $\text{Co}_2\text{Al-NO}_3(\text{ox/red})$. This value is slightly greater than the M–OH distance in the samples and allows the correlated movement of the second coordination shell to be modeled. To avoid parameters correlations, the variables were not refined simultaneously. Finally, valence bond calculations were performed to confirm the cation distribution within the hydroxide layer.³⁰ The oxidation state of the cations were estimated as follows: $v = \sum_{i=1}^n e^{(R_0-R_i)/0.37}$ where i runs through all the n bonds in the coordination sphere, with R_i individual bond lengths and R_0 bond-valence parameters (1.651 for $\text{Al}^{3+}\text{-O}$, 1.692 for $\text{Co}^{2+}\text{-O}$ and 1.70 for $\text{Co}^{3+}\text{-O}$).

3. RESULTS

3.1. Chemical and Structural Characterization of Pristine $\text{Co}_2\text{Al-NO}_3$ Sample. Powder XRD pattern of $\text{Co}_2\text{Al-NO}_3$ given in Figure 1 is typical of LDH materials with three distinct groups of reflections: (i) a series of strong basal (00l) reflections at low angles whose positions depend on the size of the intercalated anion, allowing a direct

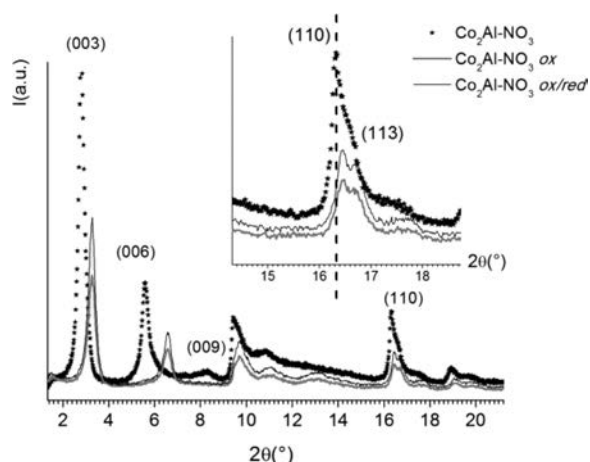


Figure 1. X-ray diffraction pattern ($\lambda = 0.4388 \text{ \AA}$) of $\text{Co}_2\text{Al-NO}_3$ sample compared to those of samples recovered after oxidation in 0.1 M KOH at a potential of 0.8 V/SCE, *i.e.*, $\text{Co}_2\text{Al-NO}_3(\text{ox})$, and submitted to further reduction at a potential of 0 V/SCE, *i.e.*, $\text{Co}_2\text{Al-NO}_3(\text{ox/red})$. The peaks are indexed considering $3R_1$ polytype.

determination of the basal spacing/interlamellar distance d , (ii) the position of the 110 reflection at high angle allowing the

value of the lattice parameter a_0 to be determined: $a_0 = 2d_{110}$ and (iii) finally, the positions of the $01l/10l$ reflections at intermediate angles which positions depend on the polytype. Generally, the $00l$ reflections of LDH are indexed as a three-layer rhombohedral polytype $3R_1$, so the value of the parameter c of the hexagonal unit cell equals $3d$. The values of the interlamellar distances d for $\text{Co}_2\text{Al-NO}_3$ estimated from the position of the $00l$ reflections is $d \sim 9.04 \text{ \AA}$, and the value of the unit cell parameter a estimated from the position of the 110 reflections is $a \sim 3.09 \text{ \AA}$. Both values are consistent with the presence of nitrate anions³¹ with a $\text{Co}^{2+}/\text{Al}^{3+}$ molar ratio close to 2.¹¹ This ratio was confirmed by ICP-AES analysis (1.99). FTIR confirms the formation of the $\text{Co}_2\text{Al-NO}_3$ LDH phase with a characteristic sharp band at 1384 cm^{-1} ($\nu_1(\text{NO}_3^-)$) and in the skeletal region the bands at 424, 547, and 609 cm^{-1} (Figure S2).³²⁻³⁴ $\text{Co}_2\text{Al-NO}_3$ was also characterized by ^{27}Al MAS NMR spectroscopy (Figure S3) in order to identify the ^{27}Al species present, as fairly large concentrations of amorphous aluminum hydroxides may be formed.³⁵ A single ^{27}Al site with an isotropic shift $\delta_{\text{iso}}(^{27}\text{Al})$ of $-689(30) \text{ ppm}$ was determined from the ^{27}Al MAS NMR spectra recorded with three different spinning speeds in agreement with usual Al octahedra as expected into the brucitic layer³⁶ and negligible quantities of diamagnetic aluminum hydroxide impurities.

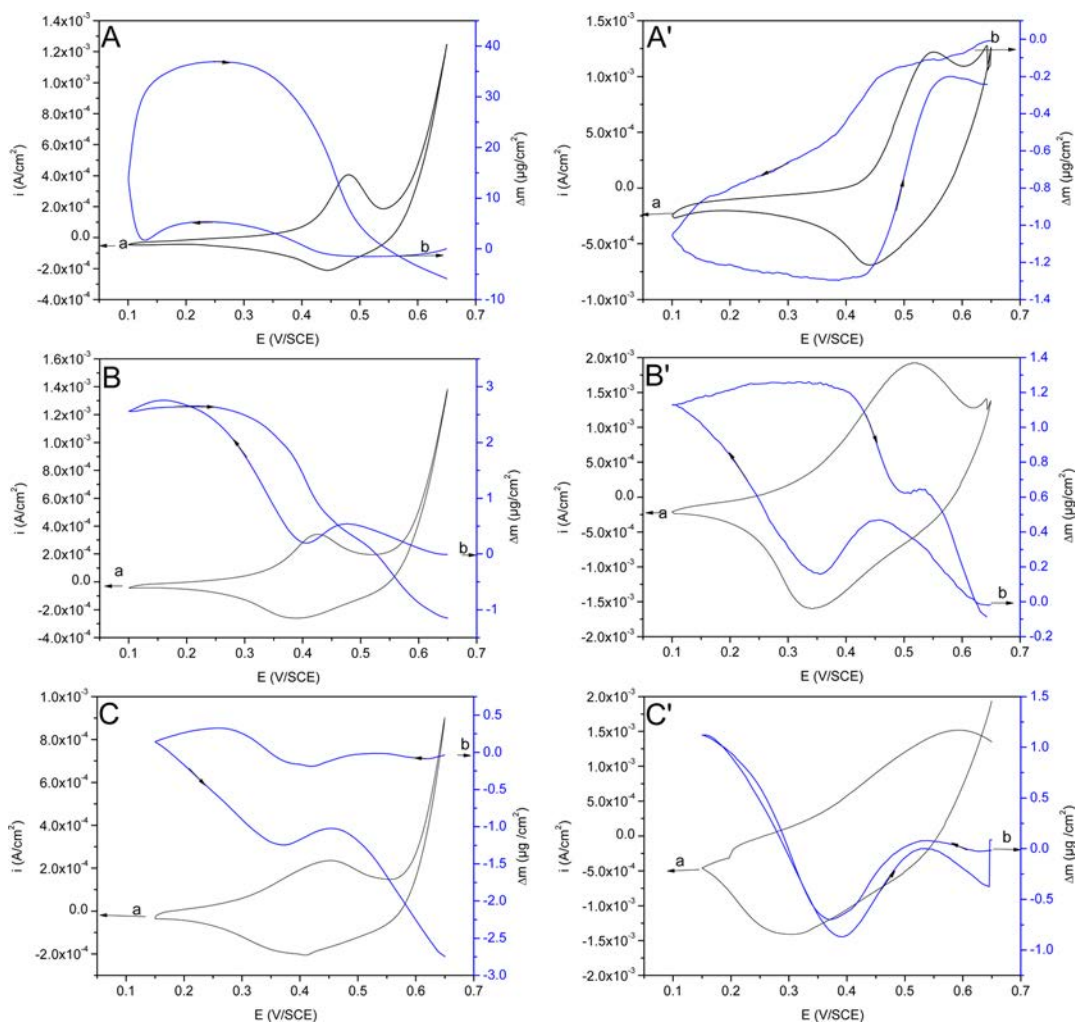


Figure 2. Cyclic voltammograms of $\text{Co}_2\text{Al-NO}_3$ films deposited on the gold electrode of the quartz resonator (curve a) and the simultaneous mass changes (curve b) in 0.1 M aqueous solutions KOH (A, A'), NaOH (B, B'), and LiOH (C, C') at $\nu = 5$ and $50 \text{ mV}\cdot\text{s}^{-1}$.

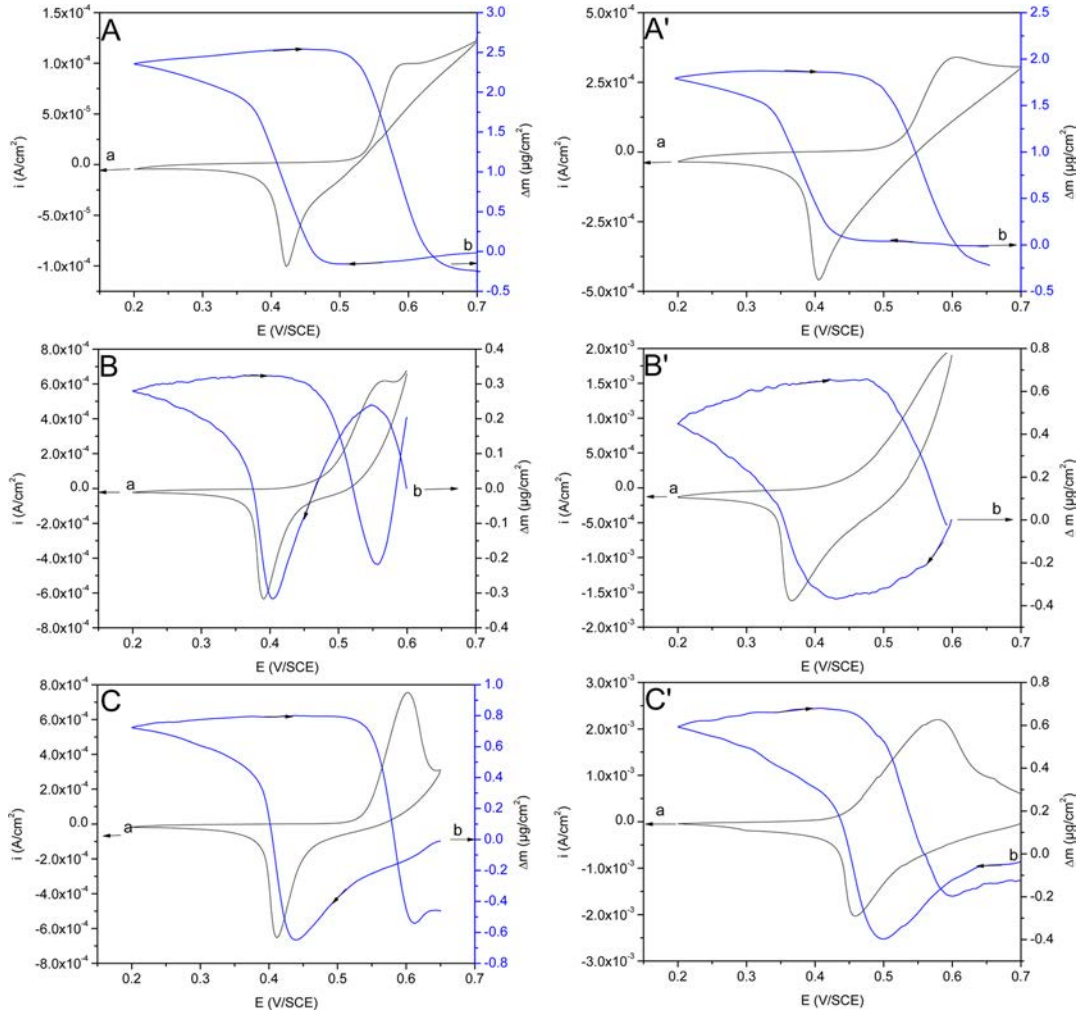


Figure 3. Cyclic voltammograms of $\text{Ni}_2\text{Al-NO}_3$ films deposited on the gold electrode of the quartz resonator (curve a) and the simultaneous mass changes (curve b) in 0.1 M aqueous solutions KOH (A, A'), NaOH (B, B'), and LiOH (C, C') at $\nu = 5$ and $50 \text{ mV}\cdot\text{s}^{-1}$.

3.2. Cyclic Electrogravimetric Studies. Figure 2 displays the cyclic voltammograms (I vs E curves) of $\text{Co}_2\text{Al-NO}_3$ films deposited on the gold electrode of the quartz resonator and the simultaneous mass changes (Δm vs E curves) in aqueous 0.1 M alkaline electrolytes. The experiments were performed at two scan rates ($\nu = 5$ and $50 \text{ mV}\cdot\text{s}^{-1}$) in three electrolytes based on three cations of different sizes: KOH, NaOH, and LiOH. A $\text{Ni}_2\text{Al-NO}_3$ sample, prepared as described by Vialat et al,¹¹ was used as a comparison (Figure 3).

The voltammograms of $\text{Co}_2\text{Al-NO}_3$ are shaped with broad signals situated at potential $E_{1/2} \approx 0.44 \text{ V}$ (Figure 2). Furthermore, the peak separations are small ($\Delta E_p = E_{p_a} - E_{p_c} \approx 30 \text{ mV}$ at $5 \text{ mV}\cdot\text{s}^{-1}$) and the ratio I_{p_a}/I_{p_c} increases from 1.1 or 1.3 in LiOH and NaOH to 1.9 in KOH. It should be mentioned that the electrochemical window for the QCM analysis should be limited to 0.55 V at $5 \text{ mV}\cdot\text{s}^{-1}$ and 0.60 V at $50 \text{ mV}\cdot\text{s}^{-1}$. This is due to the fact that the parasite reaction due to electrolyte oxidation disturbs the mass measurements, thus restricting the upper potential limit. Interestingly, the current peak intensities tend to increase linearly with the scan rate (ν) between 5 and $50 \text{ mV}\cdot\text{s}^{-1}$, except in KOH where I_{p_a} is proportional to $\nu^{1/2}$ (Figure.S4A). The number of moles of electroactive sites (n^*) can be estimated from the integration of the peaks at low scan rate (Q_a or Q_c at $\nu = 5 \text{ mV}\cdot\text{s}^{-1}$). According to the total amount of LDH coated on the electrode

surface ($50 \mu\text{g}\cdot\text{cm}^{-2}$) and the calculated molecular weight of the sample, these values can be compared to the number of moles of Co atoms present in the LDH coating (Table S1).

Cyclic voltammograms of $\text{Ni}_2\text{Al-NO}_3$ thin films deposited on gold quartz electrodes are characterized by an anodic peak and its corresponding cathodic peak at $E_{1/2} \approx 0.50 \text{ V}$ (Figure 3). This is a classical electrochemical response for this film.¹¹ As previously shown on Pt electrode, a progressive increase of Ni oxidation current signal occurs upon cycling in NaOH and LiOH solution, reaching a maximum value after several cycles (data not shown). It is noteworthy that these steady state currents obtained were much larger than that achieved in KOH, where the increase in current was significantly less important. The resulting CV curves show a peak separation $\Delta E_p \approx 200 \text{ mV}$ and a current intensity ratio (I_{p_a}/I_{p_c}) of around 1.1 in LiOH and NaOH and only 0.88 in KOH. The peak currents (I_{p_a} and I_{p_c}) were found to depend on the square root of the scan rate ($\nu^{1/2}$), suggesting a diffusion controlled reaction in LiOH and NaOH electrolyte (Figure.S4B). Interestingly, a noticeable difference in the electrochemical behavior is observed for KOH. Indeed, the slopes (I_p vs $\nu^{1/2}$) very similar between NaOH and LiOH is different in KOH, the peak intensities (I_{p_a} and I_{p_c}) are then lower and do not increase significantly with $\nu^{1/2}$. Diffusion seems to be limited in this latter electrolyte. In terms of electrochemical efficiency, more

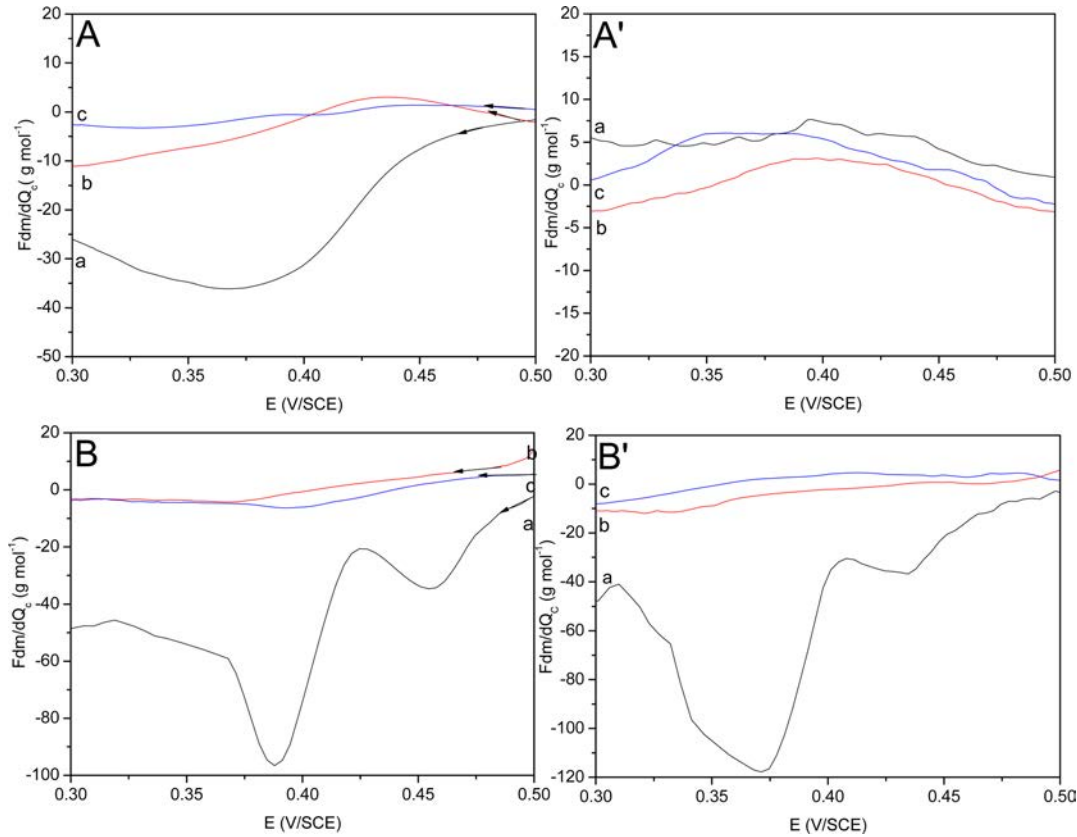


Figure 4. ($F \frac{\Delta m}{\Delta q}$) values for Co₂Al-NO₃ (A, A') and for Ni₂Al-NO₃ (B, B') as a function of the potential in 0.1 M KOH (a), NaOH (b), and LiOH (c) calculated between 0.5 and 0.3 V/SCE (at $\nu = 5 \text{ mV}\cdot\text{s}^{-1}$ (A and B) and $50 \text{ mV}\cdot\text{s}^{-1}$ (A' and B')).

electroactive sites seem accessible in cobalt-containing LDH ($\approx 29\%$ in all electrolytes) than in Ni₂Al-NO₃ (3 or 19%), except in LiOH where the percentage is comparable, $\approx 30\%$ (Table S1). However, it should be noted that the reduction of Co₂Al-NO₃ is limited in KOH with a ratio $Q_{p_a}/Q_{p_c} = 1.48$ (Table S1).

The mass responses appear different as well between both LDH materials. Indeed, a parallelogram curve shape is generally observed for Ni₂Al-LDH (Figure 3).¹⁰ For some potential values, the presence of plateaus indicates a weak electrochemical activity. The maximum of the mass-potential response slope corresponds to the anodic and cathodic peaks. Similarly to $\beta\text{-Ni}(\text{OH})_2$,³⁷ the Ni₂Al-NO₃ LDH undergoes a mass depletion during the anodic sweep and a mass increase during the cathodic sweep (Figure 3). From a global point of view, it means that, for the oxidation, cations that are expelled may be associated to solvent and a negligible counter flux of anion; for the reduction, the opposite is expected with a cation insertion also associated to a possible uptake of solvent and to a negligible counter flux of expelled anions. In term of mass changes, the most important global response is obtained in KOH electrolyte (Figure 3A) whereas in NaOH and LiOH lower values were determined.

For Co₂Al-NO₃, the rectangular curve shape of the mass response has disappeared and is replaced by wavelike curves (Figure 2). It should be mentioned that, in KOH and for the lower scan rate, the mass response is magnified 20 times compared to Ni₂Al-NO₃ films (Figure 2A). For each electrolyte, the current response is more or less similar in terms of shape while the mass response depends strongly on

the electrolyte nature: amplitude and mass/potential slope values differ strongly between the three media. Cation transfer is predominant in the three electrolytes except in KOH where, at high scan rate values, anion contribution emerges as the main input (Figure 2A'). Indeed, when the mass/potential slope is positive, cation transfer must be considered, while, for negative slope, anion motion is involved. In NaOH or LiOH, the mass variation as a function of potential was very similar upon reduction and oxidation with parallel curves showing a small hysteresis. In these electrolytes, the charge compensation mechanism seems to occur in three steps corresponding to three mass variations which become more noticeable when the scan rate increases. In all cases, the kinetic effect is observed depending on the scan rate values used. In KOH, this effect is amplified as the mass/potential slope response moves from positive to negative values at 5 and 50 mV·s⁻¹ scan rate values, respectively. For NaOH and LiOH, the mass response shape is maintained (Figure 2 B,B',C,C') but not the amplitude. The maximum is determined in KOH while a minimum mass change is depicted for NaOH and LiOH medium. This may be related to the higher molar mass of potassium compared to the other cations but also to a more efficient participation of potassium in the dynamics of transfer at the solid/solution interface.

The instantaneous molecular mass of each species can be calculated from the EQCM curves with the following relation: $F \frac{\Delta m}{\Delta q}$ in grams per mole, where F is the Faraday constant. Considering that the oxidation of Co²⁺ corresponds to one electron transfer, it should correspond to the molar mass of the

species assuring the electroneutrality during an electrochemical cycle (Figure 4). These calculations were performed in a potential window between 0.5 and 0.3 V/SCE at 5 and 50 mV·s⁻¹. EQCM curves show that electron transfer in Co₂Al–NO₃ is accompanied over the whole potential range by successive losses or gains of ionic species. Upon reduction, they may correspond to the hydroxide expulsion, the counterflux of H₂O, and finally uptake of cation.^{37,38} Here, the main contribution is due to cations transfer except at 50 mV·s⁻¹ where slightly positive values, corresponding to anions, were found in KOH and LiOH electrolytes (Figure 4A'). This difference of behavior is due to different kinetics of transfer revealed through the change of the scan rate. In KOH at 5 mV·s⁻¹, around the reduction peak (Figure 4A), $F_{\Delta q}^{\Delta m}$ corresponds to pure potassium (39 g·mol⁻¹) contributions, and apart from this potential, lower but negative $F_{\Delta q}^{\Delta m}$ values were estimated. It reveals that charge compensation is due to potassium contribution in association with a counterflux of solvent or anions. For NaOH electrolyte, the $F_{\Delta q}^{\Delta m}$ values are negative for all of the potentials, indicating a main sodium contribution. Between 0.4 and 0.45 V vs SCE, very small $F_{\Delta q}^{\Delta m}$ values are estimated to correspond to a counterflux of anion or free solvent. Finally, in LiOH only lithium ions are detected but always associated with a small counterflux of solvent as the products $F_{\Delta q}^{\Delta m}$ are estimated around 5 g·mol⁻¹. At 50 mV·s⁻¹, the $F_{\Delta q}^{\Delta m}$ values are completely different, as shown in Figure 4A'; in KOH and LiOH, only positive and small values are found, indicating an anion contribution associated with a counterflux of free solvent. From these results for Co₂Al–NO₃, given at two different scan rates, it indicates roughly that low kinetic transfers are associated with cations and, on the contrary, fast kinetic transfers are correlated to anions.

On the contrary for Ni₂Al–NO₃, the participation of K⁺ (39 g·mol⁻¹) occurs only for lower and higher potentials as the $F_{\Delta q}^{\Delta m}$ values corresponding to potassium ions are determined. Around the cathodic peak larger values are determined between 40 and 100 g·mol⁻¹. In this case, hydrated K⁺ can be considered as the main contributors to the charge compensation process. This solvation effect increases when the scan rate increases (Figure 4B'') and a maximum of hydration is obtained at 100 mV·s⁻¹ (data not shown). In the case of NaOH, sodium ions are not clearly identified for the different potentials: the calculated values are between a few grams per mole and 10 g·mol⁻¹ for potential lower than 0.4 V vs SCE (Figure 4B). Clearly, the cation contribution is demonstrated but not resulting from a mere cation transfer; a counterflux of anions is suspected in this case and for the highest potentials, $F_{\Delta q}^{\Delta m}$ present positive values which indicate a partial contribution of the OH⁻ anions (Figure 4B). This result is in good agreement with the mass response curve given in Figure 3B for the anodic potential range. The $F_{\Delta q}^{\Delta m}$ values decrease similarly to the scan rate from ≈15–11 g·mol⁻¹ at 20 or 50 mV·s⁻¹ to only 4 g·mol⁻¹ at 5 mV·s⁻¹. The same statement was reported by Villemure et al. for NiAl–Cl thin films in potassium acetate or sodium acetate where $F_{\Delta q}^{\Delta m}$ values were found to decrease along

with the scan rate.¹⁰ These low values may correspond to an average molecular weight related to the various species, and it is actually an average in terms of mass. It could be attributed to a simultaneous participation of at least two ions in the charge neutralization process with similar molecular masses, for instance insertion of Na⁺ (23 g·mol⁻¹) and expulsion OH⁻ (17 g·mol⁻¹). Finally, a molecular mass value around 6–8 g·mol⁻¹ was obtained in 0.1 M LiOH electrolyte at almost all scan rates, which is close to the molecular weight of the Li⁺ (6.9 g·mol⁻¹). It should be noted that, for the highest scan rate value (100 mV·s⁻¹, not shown here), positive $F_{\Delta q}^{\Delta m}$ values calculated around a few grams per mole; anion contribution appears here but the atomic mass of hydroxide ions is not found directly. A complex process involving free solvent, cations, and anions may explain this result. To explore more deeply the EQCM response, ac-electrogravimetric experiments might be performed. This methodology permits one to deconvolute the classical EQCM measurements given here and, very often, a more complex mechanism of charge compensation is discovered as mentioned by Escobar-Teran et al.³⁹

3.3. Structural Evolution upon Oxidation of Co₂Al–NO₃. The high electrochemical efficiency obtained with the Co₂Al–NO₃ sample led us to pay greater attention to the structure of this material and its evolution upon electrochemical treatment. To scrutinize the structures, two series of measurements were performed using high resolution X-ray synchrotron beam ($\lambda = 0.4388 \text{ \AA}$): (i) *ex situ* total scattering experiments carried out on powder samples recovered after electrolysis at constant oxidation (Co₂Al–NO₃(ox)) and reduction (Co₂Al–NO₃(ox/red)) potentials and loaded in capillaries and (ii) *operando* diffraction experiments carried out on a thin-film modified electrode (Co₂Al–NO₃/ITO) using a laboratory-made electrochemical flow cell.

3.3.1. X-ray Diffraction Analysis of *ex Situ* Samples. We first examine the X-ray diffraction signal of Co₂Al–NO₃ compared to those of *ex situ* samples, *i.e.*, Co₂Al–NO₃(ox) recovered after oxidation in KOH at a potential of 0.8 V/SCE and Co₂Al–NO₃(ox/red) submitted to further reduction at a potential of 0 V/SCE (Figure 1). All are typical of the LDH structure (see section 3.1) but significant differences are observed. For example, the position of the 00*l* diffraction peaks is shifted toward higher 2*θ* values for treated phases demonstrating a decrease of the interlamellar distance from ~9.04 Å for Co₂Al–NO₃ to 7.67 Å for Co₂Al–NO₃(ox) and Co₂Al–NO₃(ox/red). We attribute this change to replacement of nitrate anions by OH⁻ anions in the interlayer space which occurs quickly after immersion in KOH electrolyte solution. After the solids have been separated from the liquid phase, washed with water, and air-dried, the OH⁻ species are most likely replaced by CO₃²⁻ anions. Indeed, the interlayer distance of 7.67 Å is very close to that expected for carbonate-containing LDH.²³ This phase transformation is confirmed by FTIR (Figure S2). After the electrochemical treatments, the vibration band of NO₃⁻ disappears and it is replaced by a broad absorption band at 1360 cm⁻¹ on the FTIR spectra which corresponds to the ν_3 vibration of CO₃²⁻.^{32,34} At the same time, the position of the 110 reflection is slightly shifted toward higher 2*θ* for the treated samples indicating a decrease of the mean distance between adjacent cations in the hydroxide layer: $a \sim 3.09 \text{ \AA}$ for Co₂Al–NO₃ against $a \sim 3.06 \text{ \AA}$ for both Co₂Al–NO₃(ox) and Co₂Al–NO₃(ox/red). This result is consistent with an oxidation of cobalt species in Co₂Al–NO₃(ox), the

ionic radius of Co^{3+} being smaller than that of Co^{2+} . On the other hand, the fact that the distance is maintained in $\text{Co}_2\text{Al-NO}_3(\text{ox/red})$ suggests that the structural transformation is irreversible. Finally, it is interesting to note that we do not observe phase conversion upon electrochemical treatment as reported elsewhere, from $\text{Co}_2\text{Al-LDH}$ to $\gamma\text{Co}_{1-x}\text{Al}_x\text{OOH}$ (displaying an interlayer distance of $d \sim 6.89 \text{ \AA}$, a cell parameter $a \sim 2.86 \text{ \AA}$, and an IR band at 620 cm^{-1})^{14,33} and this is probably due to the different synthesis method used here to prepare $\text{Co}_2\text{Al-NO}_3$ or to the electrolyte concentration.

Important information derived from these *ex situ* X-ray diffraction data is about the presence of stacking disorder pointed out by the asymmetric broadening and the position of the reflections in the mid- 2θ region. Using DIFFax software, the patterns of highly ordered 2H_1 and 3R_1 materials were simulated and the comparison with experimental data clearly shows the occurrence of both $01l$ and $10l$ reflections characteristic of 3R_1 and 2H_1 stacking sequences, respectively (Figure 5). Therefore, the materials are likely to be an

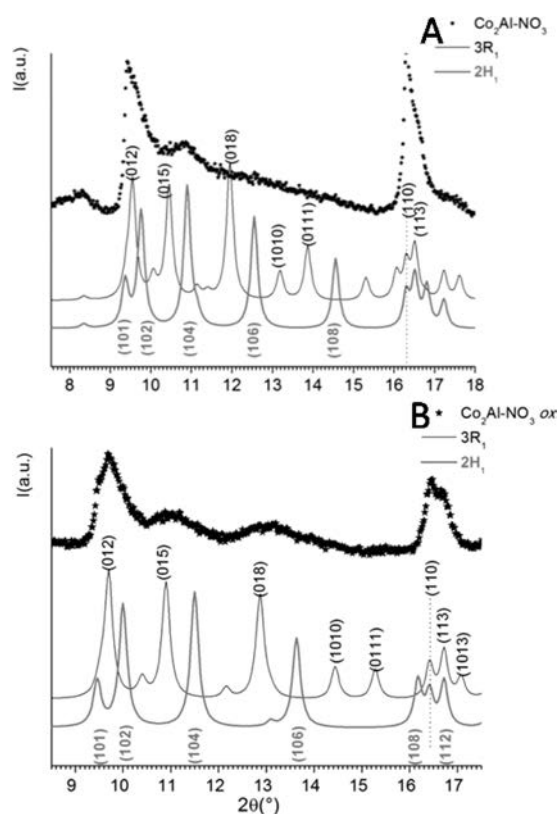


Figure 5. Experimental X-ray diffraction pattern ($\lambda = 0.4388 \text{ \AA}$) of (A) $\text{Co}_2\text{Al-NO}_3$ and (B) $\text{Co}_2\text{Al-NO}_3(\text{ox})$ (recovered after oxidation in KOH at a potential of 0.8/SCE) compared to the theoretical patterns of highly ordered 2H_1 and 3R_1 materials simulated using DIFFax software.

intergrowth between these two polytypes. Furthermore, the fact that the (110) diffraction line appears well-resolved and sharp suggests also the presence of turbostratic disorder.⁴⁰ Finally, microstructural effects such as a small size of the coherent domains and the presence of microstrains can also be put forward to fully explain the overall broad features of the XRD patterns.²³

3.3.2. Operando XRD Measurements. Operando XRD measurements were carried out during potential cycling

between 0 and 0.7 V (Figure 6). Water diffusion is responsible for the large hump observed between 5 and $15^\circ/2\theta$. ITO substrate exhibits a few Bragg reflections which are *a priori* and no longer observed when analyzing deposited LDH thin film. In agreement with *ex situ* measurements, the interlayer distance of the $\text{Co}_2\text{Al-NO}_3$ thin-film electrode quickly decreased from ~ 9.03 to $\sim 7.58 \text{ \AA}$ upon contact with the KOH electrolyte solution, which we assign to exchange of NO_3^- by OH^- implying it is under the influence of the mass action law (Figure 6A). For the starting material $\text{Co}_2\text{Al-NO}_3/\text{ITO}$, an additional reflection is observed at $4.67^\circ 2\theta$ ($\sim 5.38 \text{ \AA}$) indicated with an asterisk in Figure 6A. This peak could be ascribed to the second harmonic of the very large and asymmetrical peak centered at $\sim 9.04 \text{ \AA}$, although its position is not exactly that expected, *i.e.*, $\sim 4.52 \text{ \AA}$.

At the beginning of the application of voltage, an improvement of the crystallinity is observed leading to a net increase of the intensity of $00l$ diffraction peaks: 003 , $\sim 7.58 \text{ \AA}$; 006 , $\sim 3.73 \text{ \AA}$ (Figure 6B,C). This may be related to a migration of OH^- species enhanced by an increase of the positive charge of the hydroxide layers resulting from oxidation of Co^{2+} . Then, the crystallinity decreases continuously and the $00l$ peaks gradually split into two peaks (clearly visible on 006) leading to two interlayer distances at $3.72 \times 2 = 7.44 \text{ \AA}$ attributed to a OH^- -containing LDH phase and at $3.87 \times 2 = 7.74 \text{ \AA}$ (Figure 6C). The origin of the latter distance is uncertain and it was not observed in *ex situ* experiments (*vide supra*). For the measurements being carried out in an airtight cell, we exclude the formation of carbonate-containing LDH. Nor is it the $\beta\text{-Co}(\text{OH})_2$ ⁴¹ or $\gamma\text{-Co}_{1-x}\text{Al}_x\text{OOH}$ ¹⁴ displaying characteristic interlayer distances of 4.6 and 6.89 \AA , respectively. On the other hand, the formation of $\alpha\text{-Co}(\text{OH})_2$ phase incorporating $\text{NO}_3^-/\text{OH}^-$ interlayer anions^{42,43} as a side product of the oxidation process cannot be ruled out.

Related to the preparation of the working electrode, coated with a thin film of $\text{Co}_2\text{Al-NO}_3$, a preferential (*a*, *b*) in plane orientation of LDH crystallites was promoted, which enhances the intensity of $00l$ reflections but weakens the intensity of $hk0$ reflections, in particular the 110 reflection (Figure 6D). Therefore, it will not be possible to draw any more conclusions about the structural stability of the hydroxide layers with the present *operando* data.

3.3.3. Pair Distribution Function. Further insight into the structure of the materials and the evolution upon electrochemical treatment is obtained from PDF analysis. The total scattering structure functions $S(Q)$ and the PDF were extracted from *ex situ* data by considering both the Bragg peaks and the diffuse component; the maximum value of the wave vector Q is 23 \AA^{-1} . In Figure 7A are compared the experimental PDFs of $\text{Co}_2\text{Al-NO}_3$, $\text{Co}_2\text{Al-NO}_3(\text{ox})$, and $\text{Co}_2\text{Al-NO}_3(\text{ox/red})$.

Correlation peaks are observed up to 100 \AA although the net attenuation of the peak intensity above 30 \AA and observed in all cases may be attributed to a decreasing degree of order. For interatomic distances out to $r = 20 \text{ \AA}$, the experimental PDF of the three materials display some similarities but differences exist and are quite significant above 20 \AA (inset Figure 7A). The short-range distances for r values below the interlayer distance d mainly describe the atomic arrangements within the hydroxide layer. Indeed, owing to their low X-ray scattering power compared to Al and Co ions in the hydroxide, the contribution of interlayer species to the PDF peak is low. In this short range of interatomic distance $< d$, we find distances characteristic of LDH hydroxide layer with the first peak centered around 2.06

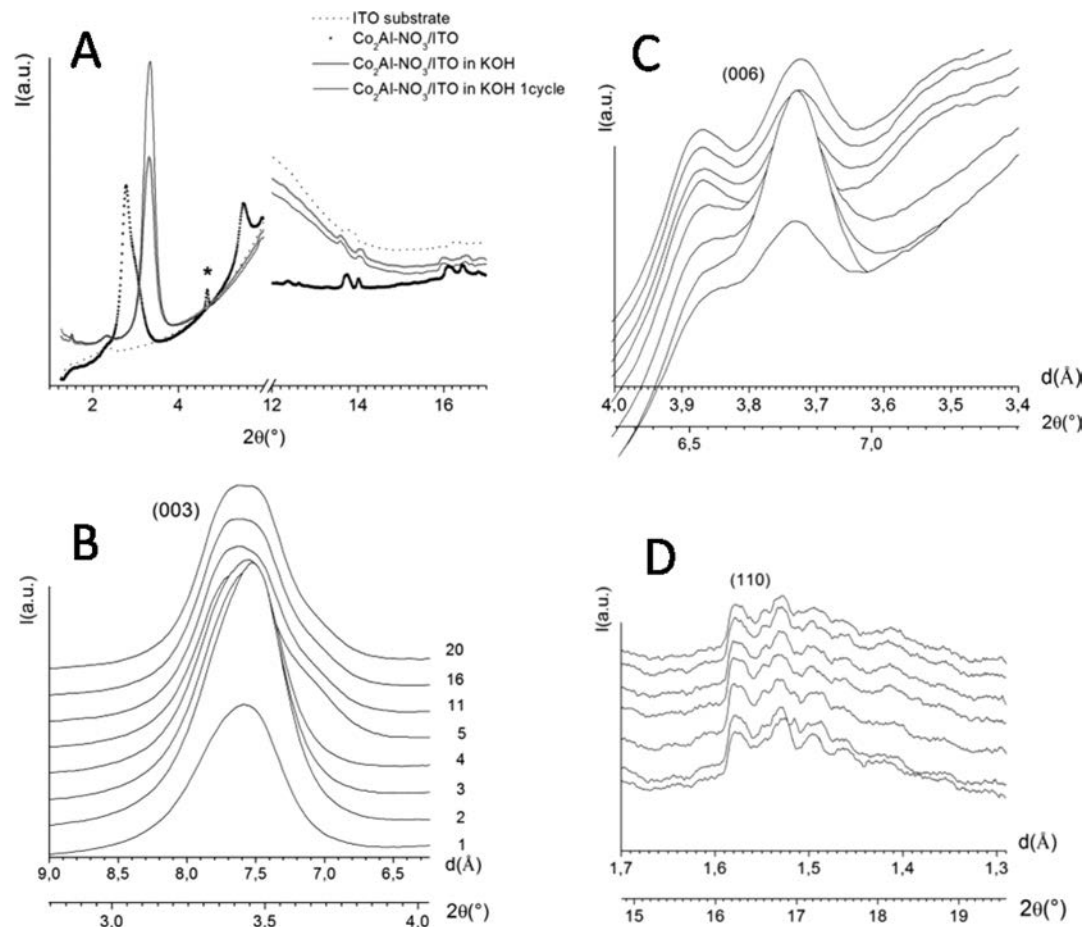


Figure 6. X-ray diffraction patterns ($\lambda = 0.4388 \text{ \AA}$) recorded during potential cycling between 0 and 0.7 V: (A) first changes observed when contacting with KOH and after one oxidation–reduction cycle (see the text for the peak noted with an asterisk); (B–D) throughout the oxidation–reduction cycles (1, 2, 3, 4, 6, 11, 16, and 20 from bottom to top) for different 2θ ranges converted into distances in angstroms.

\AA attributable to $M(\text{Co,Al})\text{--OH}$ pairs and the second one around 3.05 \AA ($\sim a$) correlated to $M\text{--}M$ distances across shared-edges octahedra, *i.e.*, the first cation coordination shell (Figure 7B). Then, the peaks observed around 5.35 \AA ($\sim a\sqrt{3}$) and 6.07 \AA ($\sim 2a$) are attributed respectively to the second and third coordination shells; finally, a layer–layer correlation peak is observed around 8.05 \AA , a value close to interlayer distance d . Interestingly for $\text{Co}_2\text{Al}\text{--NO}_3(\text{ox})$, the first peak is split into two with maxima occurring at ~ 1.94 and $\sim 1.12 \text{ \AA}$, and at the same time a slight decrease of the $M\text{--}$ distance between adjacent cations from 3.07 to 3.04 \AA is observed. This is fully consistent with the formation of Co^{3+} species upon oxidation and the appearance of short $\text{Co}^{3+}\text{--OH}$ distances. Then, for $\text{Co}_2\text{Al}\text{--O}_3(\text{ox/red})$, the first peak turns back to a single peak without modifying its position and with little or no change of the $M\text{--}M$ distance.

To extend the analysis of the PDF further, the experimental data are compared both to the calculated PDF of previously mentioned structural models, *i.e.*, $2R_1$ and $3R_1$ polytypes commonly encountered in the LDH system, and to the calculated PDF of $\text{Al}(\text{OH})_3$ gibbsite and $\beta\text{--Co}(\text{OH})_2$ and $\alpha\text{--Co}(\text{OH})_2$ phases (Figure 8). As expected and strongly suggested by the XRD patterns, neither the $3R_1$ nor the $2H_1$ structural models correctly fit the experimental PDF data at both short and longer distances for any of the samples, even after accounting for correlated atomic displacements (Figure 8A). The possible presence of $\text{Al}(\text{OH})_3$, $\beta\text{--Co}(\text{OH})_2$, or/and $\alpha\text{--}$

$\text{Co}(\text{OH})_2$ phases is also difficult to prove, especially if the PDF is the result of their intergrowth in mosaic-type domains (Figure 8B).

To get fine and quantitative information on local structural modifications occurring upon electrochemical treatment, we attempted a refinement of the PDF over the range of interatomic distance $1.5 < r/\text{\AA} < 6$ (Figure 9) where solely intralayer nearest neighbor interatomic distances are modeled, irrespective of the stacking symmetry. This range describes mainly the geometry of $M(\text{Co,Al})(\text{OH})_6$ octahedral units and allows a quantification of structural changes in the first ($M\text{--OH}$) and second ($M\text{--}M$) cation coordination shells upon electrochemical treatment.

For the refinement, a $\text{Co}_2\text{Al}(\text{OH})_6$ hydroxide layer was constructed using the structure model proposed by Marappa et al. for $\text{Zn}_2\text{Al}(\text{OH})_6 \cdot (1/2) \text{CO}_3 \cdot \text{H}_2\text{O}$.²⁸ Described in a monoclinic cell ($C2/m$ space group), this model provides two potential sites for Co,Al cation, $4g (0,y,0)$ and $2a (0,0,0)$ having the correct multiplicity ratio compared to that of $\text{Co}/\text{Al} = 2$. First, Al^{3+} was placed in the $2a$ site and Co^{2+} in the $4g$ site, leading to a cation-ordered hydroxide layer as suggested by NMR measurements (isolated $\text{Al}(\text{OH})_6$ octahedra). Detailed information on PDF refinement conditions applied here are given in the Experimental Section.

As can be seen in Figure 9, acceptable fits of the experimental data were obtained over a narrow range of distances $1.5 < r/\text{\AA} < 6$ (see also refinement results in Table 1). The refined

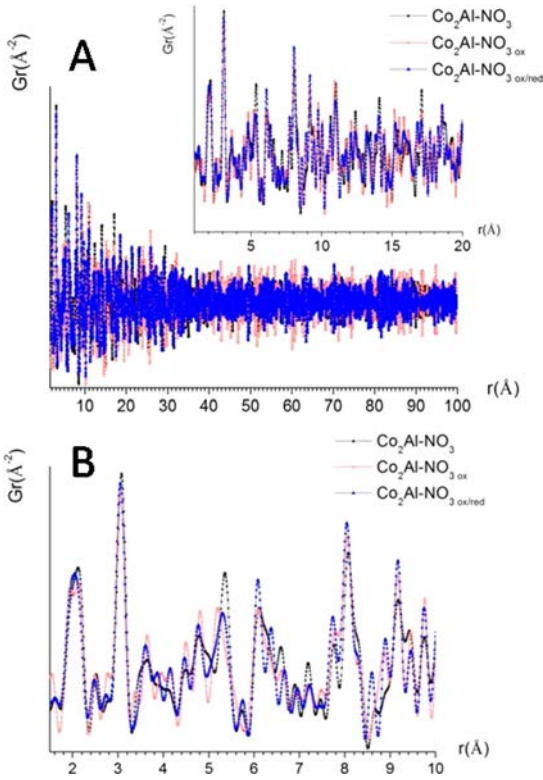


Figure 7. Extracted pair distribution function $Gr(r)$ for $\text{Co}_2\text{Al-NO}_3$ (black), $\text{Co}_2\text{Al-NO}_3(\text{ox})$ (red), and $\text{Co}_2\text{Al-NO}_3(\text{ox/red})$ (blue) from synchrotron powder X-ray diffraction data presented in different r ranges: (A) $r < 100 \text{ \AA}$ and $r < 20 \text{ \AA}$ (inset); (B) $r < 10 \text{ \AA}$ structural representation of a LDH hydroxide layer showing the main M–OH, OH–OH, and M–M distances for the first and the second coordination shells around cations.

M(Al,Co)–OH distances highlight a strongly distorted polyhedral coordination around the cations, particularly in the case of the 2a site displaying two distinctive M–OH distances at 1.744(1) and 2.062(1) Å. These distances can be first compared to Al–OH distances in gibbsite $\text{Al}(\text{OH})_3$, ranging between 1.831 and 1.924 Å, and to Co–OH distances in $\beta\text{-Co}(\text{OH})_2$, $\sim 2.097 \text{ \AA}$. Two different Al–OH bond lengths at 1.72 and 1.79 Å were also reported for $\text{Zn}_2\text{Al-CO}_3$.²⁸ Clearly, the array of hydroxyl anions does not display a hexagonal symmetry supporting the structural model chosen. As said earlier, NMR results led us to first propose a cationic ordering with the occupation of 4g and 2a sites by Co^{2+} and Al^{3+} , respectively. It is worth mentioning that we tried to lower the symmetry of the cation sites but it generated too many parameters to refine leading to unreliable values. As a consequence, a discussion on the site occupancy *versus* site symmetry is not possible in the present case. This site occupancy is somehow confirmed by bond-valence calculations:³⁰ the average valence at the 4g site assuming $\text{Co}^{2+}\text{-O}$ bonds ($R = 1.692$ bond-valence parameter) is $\langle \nu(\text{Co}) \rangle = +2.21$ and that at the 2a site is $\langle \nu(\text{Al}) \rangle = +2.87$ assuming $\text{Al}^{3+}\text{-O}$ bonds ($R = 1.651$). Yet, this strong distortion of the coordination polyhedra at the 2a site strongly suggests a mixed Co/Al occupancy. This structural order, if it exists, however, does not extend beyond $\sim 6 \text{ \AA}$, *i.e.*, next nearest neighbors as shown by the fitting result and the residual plot (Figure 9A).

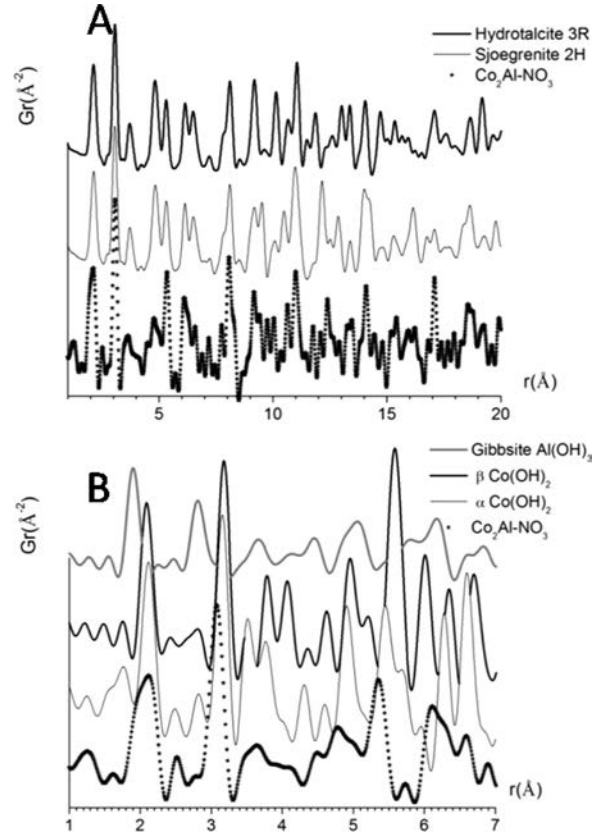


Figure 8. Experimental pair distribution function of $\text{Co}_2\text{Al-NO}_3$ compared to the calculated profiles of (A) hydrotalcite $3R_1$ and sjoegrenite $2H_1$; (B) $\text{Al}(\text{OH})_3$, $\beta\text{Co}(\text{OH})_2$, and $\alpha\text{Co}(\text{OH})_2$.

Upon application of an oxidative potential, the Co–OH distances hardly change, shorter on average; the mean variation of Co–OH distances is $\Delta\langle\text{Co-OH}\rangle = -0.012 \text{ \AA}$. In contrast, an important modification of both Al–OH distances ($\Delta\langle\text{Al-OH}\rangle = -0.026 \text{ \AA}$) and $\text{Al}(\text{OH})_6$ coordination polyhedron (more regular) was observed. This can only be ascribed to the oxidation of Co^{2+} into Co^{3+} , thus confirming the presence of Co^{2+} on the 2a site together with Al^{3+} ; Co^{2+} ions on the 2a site would then be oxidized bringing all the M–OH distances to very close values suitable for both Al^{3+} and Co^{3+} ions. On the other hand, the little change observed for the 4g site may indicate either no oxidation of Co^{2+} located on this site or an easy accommodation of different oxidation states without important structural effects. Unfortunately, it was not possible to refine $\text{Co}^{3+}/\text{Al}^{3+}$ occupancies on the 2a site under our refinement conditions. Bond-valence calculation using the average bond length $\langle\text{M-OH}\rangle$, *i.e.*, 1.930 Å, was not discriminant enough either to figure it out, leading to valences ranging from +2.98 for $\text{Co}_{0.5}\text{Al}_{0.5}$ to +2.88 for $\text{Co}_{0.2}\text{Al}_{0.8}$. However, having in mind NMR results, Al^{3+} must be in a predominant amount with respect to Co^{3+} in the 2a site. Furthermore, to be consistent with the chemical analysis of the bulk indicating a Co/Al molar ratio of 1.99, we also have to consider the presence of Al^{3+} in the 4g site but in such a very small amount that it is difficult to detect it by NMR, particularly with cobalt paramagnetic ions in large amounts in the vicinity.

Upon reduction, similarly to oxidation, we observed an important modification of the M–OH distances for the 2a site which increase in that case ($\Delta\langle\text{M-OH}\rangle = +0.038 \text{ \AA}$), obviously due to the reduction of Co^{3+} into Co^{2+} , whereas the 4g site

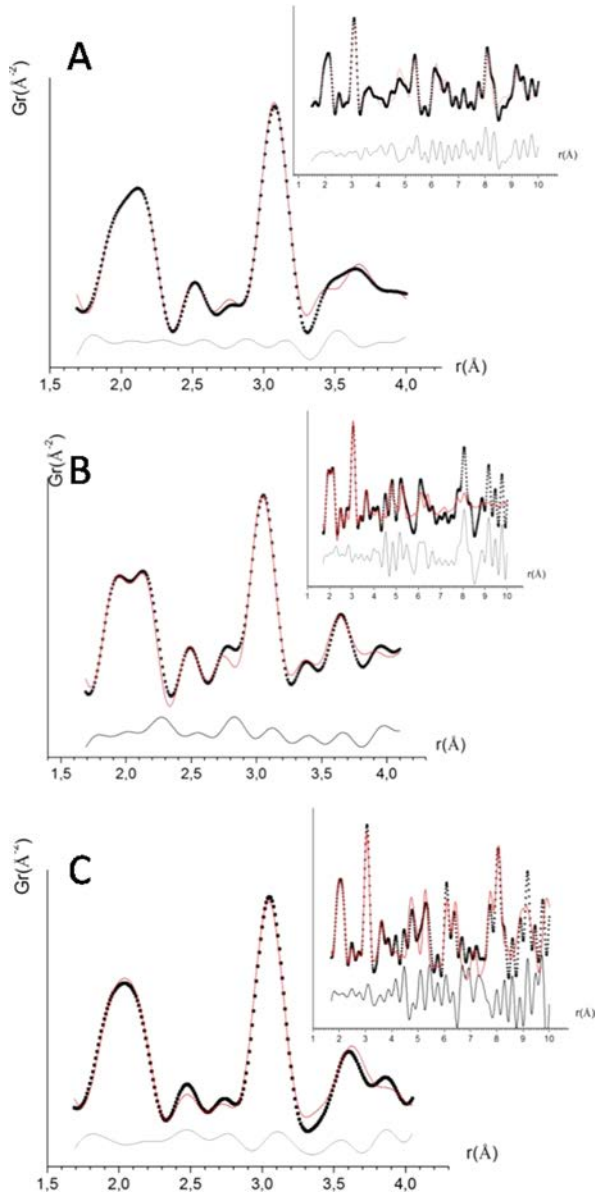


Figure 9. PDF refinement results for (A) $\text{Co}_2\text{Al-NO}_3$, (B) $\text{Co}_2\text{Al-NO}_3(\text{ox})$, and (C) $\text{Co}_2\text{Al-NO}_3(\text{ox/red})$ in the range $1.7 < r/\text{\AA} < 4$. The black stars represent the experimental data, and the red solid line corresponds to the calculated PDF; the difference curve is shown below in gray.

shows a slight decrease of Co–OH distances in average $\Delta\langle\text{Co-OH}\rangle = -0.008 \text{ \AA}$ and, as a consequence, the cell parameter a only slightly increases but not as much as one might have expected. This result may indicate that, upon oxidation, $\text{Co}_2\text{Al-LDH}$ layer structure reached steady state conditions, then enabling easy accommodation of Co in different oxidation states. It is also worth noting that, in the case of $\text{Co}_2\text{Al-NO}_3(\text{ox})$ and $\text{Co}_2\text{Al-NO}_3(\text{ox/red})$, the agreement between calculated and experimental data is observed for a narrower range of distance $r < \sim 4 \text{ \AA}$ compared to $\text{Co}_2\text{Al-NO}_3$ refinement $r < \sim 6 \text{ \AA}$ assimilated to a decrease of the size of the coherent domains and resulting from the electrochemical treatment. Therefore, the oxidation and reduction of cobalt ions would occur predominantly on the 2a site, displaying a mixed Al/Co occupancy, the ensuing structural modifications

Table 1. PDF Refinement Results for the near Interatomic Distances for $\text{Co}_2\text{Al-NO}_3$, $\text{Co}_2\text{Al-NO}_3(\text{ox})$, and $\text{Co}_2\text{Al-NO}_3(\text{ox/red})$ Considering an Ordered Arrangement of $\text{Al}(\text{OH})_6$ Polyhedra Sharing Edges with $\text{Co}(\text{OH})_6$ Polyhedra and Described in a Monoclinic Cell (Space Group $C2/m$) in Each Case^a

sample	$\text{Co}_2\text{Al-NO}_3$	$\text{Co}_2\text{Al-NO}_3(\text{ox})$	$\text{Co}_2\text{Al-NO}_3(\text{ox/red})$
refined range (\AA)	$1.5 < r < 6.0$	$1.5 < r < 4.5$	$1.5 < r < 6.0$
bond lengths (\AA)			
Co–OH	$2 \times$	$2 \times 1.924(1)$	$2 \times 1.931(1)$
/4g site	$1.940(2)$		
	$2 \times$	$2 \times 2.0876(1)$	$2 \times 2.104(1)$
	$2.120(2)$		
	$2 \times$	$2 \times 2.1726(1)$	$2 \times 2.127(1)$
	$2.160(1)$		
$\langle\text{Co-OH}\rangle$	2.074	2.062	2.054
Al–OH/2a site			
	$2 \times$	$2 \times 1.854(1)$	$2 \times 1.907(1)$
	$1.743(1)$		
	$4 \times$	$4 \times 1.9686(1)$	$4 \times 1.998(1)$
	$2.062(1)$		
$\langle\text{Al-OH}\rangle$	1.956	1.930	1.968
cell param			
a (\AA)	5.339(2)	5.275(2)	5.295(2)
b (\AA)	9.248(4)	9.150(4)	9.171(4)
c (\AA)	9.24	7.86	7.86
β (deg)	103	103	103
R_w	0.21	0.15	0.22

^aThe bond lengths listed correspond to M–OH distances in the coordination polyhedra around M cations; the numbers between parentheses are the estimated standard deviation on the last digit. The cell parameter c was not refined. The atomic coordinates and the values of the atomic displacement parameters are given in Table S2. For more details see text.

appearing reversible, at least during the first CV cycle, which explains the performances of the material.⁴⁴

4. DISCUSSION

Results of the electrogravimetry analysis show that the electrochemical process occurring within a $\text{Co}_2\text{Al-NO}_3$ modified electrode is mainly confined at the outer surface (solid/electrolyte interface) whereas the electrochemical reaction advances throughout the $\text{Ni}_2\text{Al-NO}_3$ film from the edge to the center of the film by an activation process governed by the kinetics of electron transfer and the diffusion of ions.¹¹ Indeed, the CV signals of $\text{Co}_2\text{Al-NO}_3$, which take place at a lower potential with slightly low values of ΔE_p ($\sim 30 \text{ mV}$), are similar to reversible thin-layer voltammograms. Moreover, EQCM curves show that an electron transfer in $\text{Co}_2\text{Al-NO}_3$ is characterized over the whole potential range by successive losses or gains of ionic species which may be hydroxides, H_2O , and cations.^{37,38} In both experiments (CV and EQCM), the influence of the scan rate is minimized. Nevertheless, separating the contribution between anion, cation, and free solvent using this method of film characterization is challenging.

According to the theoretical models offered by Lovric, Scholz, Oldham, and co-workers,^{9,45–47} electrochemical behavior within porous solids is a function of the individual diffusion coefficient of electrons (D_e) and ions (D_i) within the materials. They described an electrochemical reaction within immobilized microcrystals assuming that the redox reaction is initiated at the electrolyte/solid/electrode three-phase junction and then

expands through the solid *via* electron hopping between immobile redox centers and ion diffusion through the solid, leading to a progressive growing of the reaction zone, as observed in the case of Ni₂Al–NO₃.¹¹

Under certain conditions, a transition of the three-phase reaction to a pure two-phase reaction occurs, in particular when electrons move quickly along the material and the ion diffusion through the solid/electrolyte interface is slower. In this case, a film of oxidized product also appears at the outer surface of the material, with an accumulation of ions at the solid/electrolyte interface. It is probably why the interlayer layer space is not affected along potential cycling.

This means that the faradic process regarding its surface component may be defined more like a pseudocapacitive behavior. This is probably what happens in Co₂Al–NO₃ for which a pseudocapacitive behavior was found, using electrochemical impedance and galvanostatic measurements.¹¹ Indeed, the charge capacity at 1 A·g⁻¹ in KOH is 340 F·g⁻¹ (190 F·g⁻¹ for discharge) for Co₂Al–NO₃, whereas it is only 5 F·g⁻¹ (3 F·g⁻¹ for discharge) for Ni₂Al–NO₃ (Figure S5). Moreover, these specific capacitances are cation size dependent in Ni₂Al–NO₃ films, while the effect of electrolyte cation is obviously less significant for Co₂Al–NO₃-based LDH film.¹¹

Those results are consequently in favor of a progressive activation process in the case of Ni₂Al–NO₃ against a multisite process for Co₂Al–NO₃. This main difference between both materials may have its origin in structural differences. Indeed in a previous work, we have shown that the electrochemical behavior of Ni₂Al–CO₃ LDH is a result of competing effects between the coherent domain size, the particle size, the aggregation state of LDH particles, the Ni bulk concentration, and the presence of structural defects.²³ Remarkably, the presence of the 2H₁ stacking patterns in the 3R₁ in those NiAl–LDH matrices results in an increased electrochemical signal.

Therefore, the atypical pseudocapacitive response of Co₂Al–NO₃ material led us to examine in detail its structure and evolution upon oxidation. As a result of the synthesis method used, *i.e.*, coprecipitation method in so-called “fast” conditions, the crystallinity of the starting phase is quite low, leading to broad X-ray diffraction peaks indicative of a small size of the coherent domains and the presence of disorder. In particular, the presence of both 3R₁ and 2H₁ polytypes is highly probable. The same powder sample recovered after oxidative electrolysis (at a constant potential) clearly shows a decrease of the mean distance between adjacent cations within the hydroxide layer ($2d_{110}$) consistently with the oxidation of Co²⁺ and the formation of shorter Co³⁺–OH distances.

Operando measurements carried out on thin films in KOH electrolyte allowed us to observe the diffusion of OH⁻ species gradually replacing NO₃⁻. After several CV cycles, the material separates into two lamellar phases with two distinct interlayer distances, attributed to a OH⁻-containing LDH and α -Co(OH)₂, respectively.

PDF data, obtained from the analysis of the total scattering patterns, provide a more accurate picture of the structure, probing local and long-range structure simultaneously. Consistently with the presence of many kinds of disorder (stacking faults, interstratification), the experimental PDF are very different from those expected for the average structures of 3R₁ and 2H₁ polytypes. Only locally, for $r < 6$ Å, *i.e.*, interatomic distances between nearest and next nearest neighbors within the hydroxide layers, there is some semblance of agreement with the experimental data and the calculated

profiles for a layer of edge-sharing octahedra. On the other hand, this analysis is very sensitive to the local structural modification within the hydroxide layer induced by the electrochemical treatment. Starting from the structure model proposed by Marappa and Kamath considering a monoclinic symmetry,²⁸ refinement of the PDFs in the short-range $r < 6$ Å was carried out. In this range of distance, only intralayer pairwise interactions are modeled and those concern only the first and second coordination sphere around M cations. Acceptable fits of the experimental data were obtained by considering an ordered arrangement of strongly distorted Al(OH)₆ polyhedra sharing edges with larger and more regular Co(OH)₆ octahedra. This local ordering below ~ 6 Å suggests the presence of clusters of layered double metal hydroxides randomly distributed. The strong distortion of Al(OH)₆ polyhedra is likely to be due to the presence of Co²⁺ sharing the same site, although it has not been possible to quantify it. A variation of M–OH distances is observed upon electrochemical treatment consistently with first an oxidation of Co²⁺ into Co³⁺ ($\Delta\langle M-OH \rangle = -0.012$ Å/ -0.026 Å for 4g/2a sites) and then a reduction Co³⁺ into Co²⁺ ($\Delta\langle M-OH \rangle = -0.008$ Å/ $+0.038$ Å for 4g/2a sites). The structural changes associated with the electrochemical phenomena are more visible on the site displaying a mixed Co/Al occupancy, thus able to accommodate different bond lengths, and we think that the ~ 20 – 30% of electroactive Co species determined by CV (Table 1) are mainly located on this site. This result is in full agreement with the assumption that Wang et al. made, namely, that “the partial isomorphous substitution of Co²⁺ by Al³⁺ favors the retention of the original layered structure during the redox reaction”.⁴⁴ The pseudocapacitive performances of the material certainly results from the easy accommodation of different oxidation states in LDH structure, but we are also tempted to say that the presence of clusters may also contribute to the electroactivity of the material.

5. CONCLUSION

We emphasize the power of the *operando* methods used here, namely, EQCM and XRD, for establishing structure–electrochemical property correlations in a functional materials layered structure. EQCM results show larger current densities and mass responses for Co₂Al–NO₃ in comparison to Ni₂Al–NO₃. Moreover, the electrochemical process depends noticeably on the nature of electrolyte cations for Ni₂Al–NO₃, whereas it is less significant for Co₂Al–NO₃. This suggests that the electrochemical reaction advances throughout the Ni₂Al–NO₃ film by a collective process governed by the kinetics of electron transfer, whereas it is mainly confined at the outer surface of Co₂Al–NO₃ film leading to its pseudocapacitive behavior.

Even if PDF analysis is known as a powerful method to scrutinize electrochemical conversion and electrogrinding effects involving significant local order and interatomic distances changes upon oxidation and reduction,^{48,49} little was reported for small changes occurring in supercapacitor-type devices. Indeed this study points out the relevance of PDF analyses for more subtle changes as encountered in this study, underlining the importance of verifying the synthesis conditions. The average structure as observed by classical powder XRD analysis and often assimilated to a LDH structure may actually conceal countless structural defects and structural heterogeneities as shown by the PDF analysis. Such a situation is highly probable when using fast precipitation methods with

important outcomes on the interpretation of physical measurements of the bulk.

AUTHOR INFORMATION

Corresponding Authors

*(C.M.) E-mail: Christine.Mousty@univ-bpclermont.fr.

*(C.T.-G.) E-mail: Christine.Taviot-Gueho@univ-bpclermont.fr.

*(H.P.) E-mail: hubert.perrot@upmc.fr.

Notes

The authors declare no competing financial interest.

ACKNOWLEDGMENTS

U.G.N. and N.D.J. are grateful for financial support from the Villum Foundation via the "Villum Young Investigator Program" Grant VKR022364 and for use of SSNMR equipment (Villum Center for Bioanalytical Services, 600 MHz NMR instrument). U.G.N., N.D.J., and C.M. acknowledge funding from Institut Français du Danemark. Clémence Bigot and Michael Herraiz are also acknowledged for their experimental help.

REFERENCES

(1) Akinyele, D. O.; Rayudu, R. K. Review of energy storage technologies for sustainable power networks. *Sustain. Energy Technol. Assess.* **2014**, *8*, 74–91.

(2) Luo, X.; Wang, J.; Dooner, M.; Clarke, J. Overview of current development in electrical energy storage technologies and the application potential in power system operation. *Appl. Energy* **2015**, *137*, 511–536.

(3) Mousty, C.; Leroux, F. LDHs as Electrode Materials for Electrochemical Detection and Energy Storage: Supercapacitor, Battery and (Bio)-Sensor. *Recent Pat. Nanotechnol.* **2012**, *6*, 174–192.

(4) Shao, M. F.; Zhang, R. K.; Li, Z. H.; Wei, M.; Evans, D. G.; Duan, X. Layered double hydroxides toward electrochemical energy storage and conversion: design, synthesis and applications. *Chem. Commun.* **2015**, *51*, 15880–15893.

(5) Wang, J.; Wang, L.; Chen, X.; Lu, Y.; Yang, W. Chemical power source based on layered double hydroxides. *J. Solid State Electrochem.* **2015**, *19*, 1933–1948.

(6) Wang, Q.; O'Hare, D. Recent advances in the synthesis and application of layered double hydroxide (LDH) nanosheets. *Chem. Rev.* **2012**, *112*, 4124–4155.

(7) Mousty, C.; Prevot, V. Hybrid and biohybrid layered double hydroxides for electrochemical analysis. *Anal. Bioanal. Chem.* **2013**, *405*, 3513–3523.

(8) Vialat, P.; Leroux, F.; Mousty, C. Electrochemical properties of layered double hydroxides containing 3d metal cations. *J. Solid State Electrochem.* **2015**, *19*, 1975–1983.

(9) Lovrić, M.; Scholz, F. A model for the propagation of a redox reaction through microcrystals. *J. Solid State Electrochem.* **1997**, *1*, 108–113.

(10) Roto, R.; Yamagishi, A.; Villemure, G. Electrochemical quartz crystal microbalance study of mass transport in thin film of a redox active Ni-Al-Cl layered double hydroxide. *J. Electroanal. Chem.* **2004**, *572*, 101–108.

(11) Vialat, P.; Leroux, F.; Taviot-Gueho, C.; Villemure, G.; Mousty, C. Insights into the electrochemistry of $(\text{Co}_x\text{Ni}_{1-x})_2\text{Al}-\text{NO}_3$ Layered Double Hydroxides. *Electrochim. Acta* **2013**, *107*, 599–610.

(12) Yao, K.; Taniguchi, M.; Nakata, M.; Shimazu, K.; Takahashi, M.; Yamagishi, A. Mass transport on an anionic clay-modified electrode as studied by a quartz crystal microbalance. *J. Electroanal. Chem.* **1998**, *457*, 119–128.

(13) Roto, R.; Villemure, G. Mass transport in thin films of $[\text{Fe}(\text{CN})_6]^{4-}$ exchanged Ni-Al layered double hydroxide monitored with an electrochemical quartz crystal microbalance. *J. Electroanal. Chem.* **2006**, *588*, 140–146.

(14) Scavetta, E.; Ballarin, B.; Corticelli, C.; Gualandi, I.; Tonelli, D.; Prevot, V.; Forano, C.; Mousty, C. An insight into the electrochemical behavior of Co/Al layered double hydroxide thin films prepared by electrodeposition. *J. Power Sources* **2012**, *201*, 360–367.

(15) Sauerbrey, G. Verwendung von Schwingquarzen zur Waigung dünner Schichten und zur aMikrowaigung. *Eur. Phys. J. A* **1959**, *155*, 206–222.

(16) Agrisuelas, J.; Gabrielli, C.; Garcia-Jareno, J. J.; Gimenez-Romero, D.; Gregori, J.; Perrot, H.; Vicente, F. Usefulness of $F(\text{dm}/\text{dQ})$ function for elucidating the ions role in PB films. *J. Electrochem. Soc.* **2007**, *154*, F134–F140.

(17) Calvo, E.; Kanazawa, K.; Perrot, H.; Jimenez, Y. Combination of Quartz Crystal Microbalance with Other Techniques. In *Piezoelectric Transducers and Applications*; Vives, A. A., Ed.; Springer-Verlag: Berlin, Heidelberg, 2008; pp 307–330, DOI: 10.1007/978-540-77508-9_13.

(18) García-Jareño, J. J.; Gabrielli, C.; Perrot, H. Validation of the mass response of a quartz crystal microbalance coated with Prussian Blue film for ac electrogravimetry. *Electrochem. Commun.* **2000**, *2*, 195–200.

(19) Bizet, K.; Gabrielli, C.; Perrot, H. Immunodetection by quartz crystal microbalance. *Appl. Biochem. Biotechnol.* **2000**, *89*, 139–149.

(20) Ndjeri, M.; Peulon, S.; Schlegel, M. L.; Chausse, A. In situ grazing-incidence X-ray diffraction during electrodeposition of birnessite thin films: Identification of solid precursors. *Electrochem. Commun.* **2011**, *13*, 491–494.

(21) Treacy, M. M. J.; Newsam, J. M.; Deem, M. W. A. A general recursion method for calculating diffracted intensities from crystal containing planar faults. *Proc. R. Soc. London, Ser. A* **1991**, *433*, 499–520.

(22) Radha, S.; Kamath, P. V. Structural Synthon Approach to Predict the Possible Polytypes of Layered Double Hydroxides. *Z. Anorg. Allg. Chem.* **2012**, *638*, 2317–2323.

(23) Faour, A.; Mousty, C.; Prevot, V.; Devouard, B.; De Roy, A.; Bordet, P.; Elkaim, E.; Taviot-Gueho, C. Correlation among Structure, Microstructure, and Electrochemical Properties of NiAl-CO₃ Layered Double Hydroxide Thin Films. *J. Phys. Chem. C* **2012**, *116*, 15646–15659.

(24) Marappa, S.; Radha, S.; Kamath, P. V. Nitrate-Intercalated Layered Double Hydroxides – Structure Model, Order, and Disorder. *Eur. J. Inorg. Chem.* **2013**, *2013*, 2122–2128.

(25) Billinge, S. J. L. Nanoscale structural order from the atomic pair distribution function (PDF): There's plenty of room in the middle. *J. Solid State Chem.* **2008**, *181*, 1695–1700.

(26) Qiu, X.; Thompson, J. W.; Billinge, S. J. L. PDFgetX2: a GUI-driven program to obtain the pair distribution function from X-ray powder diffraction data. *J. Appl. Crystallogr.* **2004**, *37*, 678.

(27) Juhas, P.; Davis, T.; Farrow, C. L.; Billinge, S. J. L. PDFgetX3: a rapid and highly automatable program for processing powder diffraction data into total scattering pair distribution functions. *J. Appl. Crystallogr.* **2013**, *46*, S60–S66.

- (28) Marappa, S.; Kamath, P. V. Structure of the Carbonate-Intercalated Layered Double Hydroxides: A Reappraisal. *Ind. Eng. Chem. Res.* **2015**, *54*, 11075–11079.
- (29) Proffen, T.; Billinge, S. J. L. PDFFIT, a program for full profile structural refinement of the atomic pair distribution function. *J. Appl. Crystallogr.* **1999**, *32*, 572–575.
- (30) Brese, N. E.; O'Keefe, M. Bond-valence parameters for solids. *Acta Crystallogr., Sect. B: Struct. Sci.* **1991**, *47*, 192–197.
- (31) Forano, C.; Costantino, U.; Prevot, V.; Taviot-Gueho, C. Layered Double Hydroxides (LDH). In *Handbook of Clay Science*, 2nd ed.; Bergaya, F., Lagaly, G., Eds.; Elsevier: Oxford, U.K., 2013; Chapter 14.1, Vol. 5A, Developments in Clay Science, pp 745–782.
- (32) Klopogge, J. T.; Frost, R. L. Infrared and Raman spectroscopic studies of layered double hydroxides (LDHs). In *Layered Double Hydroxydes: Present and Future*, Rives, V., Ed.; Nova Science: New York, 2001; pp 139-192.
- (33) Wang, Y.; Yang, W. S.; Zhang, S. C.; Evans, D. G.; Duan, X. Synthesis and electrochemical characterization of Co-Al layered double hydroxides. *J. Electrochem. Soc.* **2005**, *152*, A2130–A2137.
- (34) Kannan, S.; Swamy, C. S. Synthesis and physicochemical characterization of cobalt aluminium hydroxalcite. *J. Mater. Sci. Lett.* **1992**, *11*, 1585–1587.
- (35) Pushparaj, S. S. C.; Forano, C.; Prevot, V.; Lipton, A. S.; Rees, G. J.; Hanna, J. V.; Nielsen, U. G. How the Method of Synthesis Governs the Local and Global Structure of Zinc Aluminum Layered Double Hydroxides. *J. Phys. Chem. C* **2015**, *119*, 27695–27707.
- (36) Sideris, P. J.; Nielsen, U. G.; Gan, Z. H.; Grey, C. P. Mg/Al Ordering in Layered Double Hydroxides Revealed by Multinuclear Nmr Spectroscopy. *Science* **2008**, *321*, 113–117.
- (37) Wehrens-Dijksma, M.; Notten, P. H. L. Electrochemical Quartz Microbalance characterization of Ni(OH)₂-based thin film electrodes. *Electrochim. Acta* **2006**, *51*, 3609–3621.
- (38) French, H. M.; Henderson, M. J.; Hillman, A. R.; Viel, E. Ion and solvent transfer discrimination at a nickel hydroxide film exposed to LiOH by combined electrochemical quartz crystal microbalance (EQCM) and probe beam deflection (PBD) techniques. *J. Electroanal. Chem.* **2001**, *500*, 192–207.
- (39) Escobar-Teran, F.; Arnau, A.; Garcia, J. V.; Jiménez, Y.; Perrot, H.; Sel, O. Gravimetric and dynamic deconvolution of global EQCM response of carbon nanotube based electrodes by Ac-electrogravimetry. *Electrochem. Commun.* **2016**, *70*, 73–77.
- (40) Thomas, G. S.; Kamath, P. V. Line broadening in the PXRD patterns of layered hydroxides: The relative effects of crystallite size and structural disorder. *Proc. - Indian Acad. Sci., Chem. Sci.* **2006**, *118*, 127–133.
- (41) Wyckoff, R. W. G. *Crystal Structures*; Interscience: New York, 1963; Vol. 1, pp 239–444.
- (42) Ma, R.; Liu, Z.; Takada, K.; Fukuda, K.; Ebina, Y.; Bando, Y.; Sasaki, T. Tetrahedral Co(II) Coordination in α -Type Cobalt Hydroxide: Rietveld Refinement and X-ray Absorption Spectroscopy. *Inorg. Chem.* **2006**, *45*, 3964–3969.
- (43) Rajamathi, M.; Kamath, P.; Seshadri, R. Chemical synthesis of α -cobalt hydroxide. *Mater. Res. Bull.* **2000**, *35*, 271–278.
- (44) Wang, Y.; Yang, W.; Chen, C.; Evans, D. G. Fabrication and electrochemical characterization of cobalt-based layered double hydroxide nanosheet thin-film electrodes. *J. Power Sources* **2008**, *184*, 682–690.
- (45) Lovrić, M.; Hermes, M.; Scholz, F. The effect of the electrolyte concentration in the solution on the voltammetric response of insertion electrodes. *J. Solid State Electrochem.* **1998**, *2*, 401–404.
- (46) Schröder, U.; Oldham, K. B.; Myland, J. C.; Mahon, P. J.; Scholz, F. Modelling of solid state voltammetry of immobilized microcrystals assuming an initiation of the electrochemical reaction at a three-phase junction. *J. Solid State Electrochem.* **2000**, *4*, 314–324.
- (47) Oldham, K. B. Voltammetry at a three-phase junction. *J. Solid State Electrochem.* **1998**, *2*, 367–377.
- (48) Shyam, B.; Chapman, K. W.; Balasubramanian, M.; Klingler, R. J.; Srajer, G.; Chupas, P. J. Structural and Mechanistic Revelations on an Iron Conversion Reaction from Pair Distribution Function Analysis. *Angew. Chem., Int. Ed.* **2012**, *51*, 4852–4855.
- (49) Wang, F.; Robert, R.; Chernova, N. A.; Pereira, N.; Omenya, F.; Badway, F.; Hua, X.; Ruotolo, M.; Zhang, R.; Wu, L.; Volkov, V.; Su, D.; Key, B.; Whittingham, M. S.; Grey, C. P.; Amatucci, G. G.; Zhu, Y.; Graetz, J. Conversion Reaction Mechanisms in Lithium Ion Batteries: Study of the Binary Metal Fluoride Electrodes. *J. Am. Chem. Soc.* **2011**, *133*, 18828–18836.